APL Materials

RESEARCH ARTICLE | JUNE 22 2023

Mapping the complex evolution of ferroelastic/ferroelectric domain patterns in epitaxially strained $PbTiO_3$ heterostructures

Céline Lichtensteiger ; Marios Hadjimichael ; Edoardo Zatterin ; Chia-Ping Su ; Iaroslav Gaponenko ; Ludovica Tovaglieri ; Patrycja Paruch ; Alexandre Gloter ; Jean-Marc Triscone

APL Mater 11, 061126 (2023)
https://doi.org/10.1063/5.0154161

APL Materials ARTICLE pubs.aip.org/aip/apm

Mapping the complex evolution of ferroelastic/ferroelectric domain patterns in epitaxially strained $PbTiO_3$ heterostructures

Cite as: APL Mater. 11, 061126 (2023); doi: 10.1063/5.0154161
Submitted: 13 April 2023 • Accepted: 6 June 2023 •
Published Online: 22 June 2023

Céline Lichtensteiger,[1,a)] Marios Hadjimichael,[1] Edoardo Zatterin,[2] Chia-Ping Su,[3] Iaroslav Gaponenko,[1] Ludovica Tovaglieri,[1] Patrycja Paruch,[1] Alexandre Gloter,[3] and Jean-Marc Triscone[1]

AFFILIATIONS

[1] Department of Quantum Matter Physics, University of Geneva, 24 Quai Ernest-Ansermet, CH-1211 Geneva 4, Switzerland
[2] ESRF, The European Synchroton, 71 Avenue des Martyrs, Grenoble 38000, France
[3] CNRS, Laboratoire de Physique des Solides, Université Paris-Saclay, Orsay 91405, France

[a)] **Author to whom correspondence should be addressed:** Celine.Lichtensteiger@unige.ch

ABSTRACT

We study the complex ferroelastic/ferroelectric domain structure in the prototypical ferroelectric $PbTiO_3$ epitaxially strained on $(110)_o$-oriented $DyScO_3$ substrates, using a combination of atomic force microscopy, laboratory and synchrotron x-ray diffraction, and high resolution scanning transmission electron microscopy. We observe that the anisotropic strain imposed by the orthorhombic substrate creates a large asymmetry in the domain configuration, with domain walls macroscopically aligned along one of the two in-plane directions. We show that the periodicity as a function of film thickness deviates from the Kittel law. As the ferroelectric film thickness increases, we find that the domain configuration evolves from flux-closure to a/c-phase, with a larger scale arrangement of domains into superdomains.

I. INTRODUCTION

In ferroelectric thin films, the interplay between mechanical and electrostatic boundary conditions allows for the formation of a large variety of domain structures with fascinating properties. This is particularly the case in $PbTiO_3$, a tetragonal ferroelectric with polarization developing along the c axis mostly due to ionic displacements. In $PbTiO_3$ thin films, the orientation of the polarization and arrangement into domain structures have been theoretically studied[1–6] and are described as phase diagrams with regions of different domain configurations as a function of epitaxial strain and temperature (see review by Schlom *et al.*[7]). When the electrostatic boundary conditions are modified and the depolarization field is introduced, the polarization configurations in $PbTiO_3$ become more complex; for example, in $PbTiO_3/SrTiO_3$ superlattices, which are periodic repetitions of $PbTiO_3$ and $SrTiO_3$ deposited on $DyScO_3$ substrates, the ferroelectric layers display ordered arrays of polar vortices.[8] Additionally, the signature of Bloch polarization components was observed using resonant soft x-ray diffraction (RSXD).[9] A "supercrystal" structure of very ordered flux closure domains was stabilized using ultrafast light pulses,[10] a configuration somewhat similar to the spontaneously ordered phase observed in $PbTiO_3/SrRuO_3$ superlattices deposited on $DyScO_3$.[11,12] An incommensurate spin crystal was observed in $PbTiO_3$ thin films between $SrRuO_3$ electrodes on $DyScO_3$.[13] Ferroelectric skyrmions were predicted in $PbTiO_3$[14] and subsequently measured in $PbTiO_3/SrTiO_3$ superlattices on $SrTiO_3$ substrates,[15] and polar merons were observed in mixed $a_1/a_2 - a/c$ phase $PbTiO_3$ films under tensile epitaxial strain on a $SmScO_3$ substrate.[16] All these observations demonstrate that the interplay between elastic and electrostatic energies creates structures, which can be simultaneously controlled using electric fields and light and give rise to

novel phenomena, like negative capacitance.[17] The studied systems are usually complicated and are characterized by mixed phases of different domain configurations.[18]

In this work, a series of samples were grown by off-axis radio frequency (RF) magnetron sputtering on $(110)_o$-oriented $DyScO_3$ substrates, with 55 unit cells (u.c.) thick bottom and top $SrRuO_3$ electrodes and $PbTiO_3$ film thicknesses ranging from 23 up to 133 u.c. (see Sec. V A for details regarding sample growth). To understand the domain configuration in such samples, both the elastic strain and electrostatic boundary conditions must be considered.

Bulk $PbTiO_3$ is ferroelectric below a critical temperature of 765 K, with a tetragonal structure and lattice parameters $a = b = 3.904$ Å and $c = 4.152$ Å at room temperature.[19] $DyScO_3$ is orthorhombic with room temperature *Pbnm* space group lattice parameters[20] $a_o = 5.443(2)$ Å, $b_o = 5.717(2)$ Å, and $c_o = 7.901(2)$ Å, corresponding to pseudocubic lattice parameters $a_{pc} = c_{pc} = \frac{\sqrt{a_o^2+b_o^2}}{2} = 3.947$ Å, $b_{pc} = c_o/2 = 3.951$ Å, $\alpha_{pc} = \gamma_{pc} = 90°$, and $\beta_{pc} = 2 \cdot \arctan(a_o/b_o) = 87.187°$. For $(110)_o$-oriented $DyScO_3$, the out-of-plane $[001]_{pc}$ direction is equivalent to $[110]_o$, while the in-plane directions $[100]_{pc}$ and $[010]_{pc}$ are equivalent to $[\bar{1}10]_o$ and $[001]_o$, respectively (the subscript "*pc*" refers to the pseudocubic unit cell, while "*o*" is used to refer to the orthorhombic unit cell). In our sample series, the in-plane strain imposed by $DyScO_3$ on $PbTiO_3$ films at room temperature can thus be calculated as $\frac{a_{pc}-a_0}{a_{pc}} = -0.25\%$ along $[100]_{pc}$ and $\frac{b_{pc}-a_0}{b_{pc}} = -0.16\%$ along $[010]_{pc}$, where $a_0 = 3.957$ Å is the equivalent lattice parameter of $PbTiO_3$ in the room-temperature cubic paraelectric phase. To accommodate this strain, $PbTiO_3$ thin films on $DyScO_3$ are expected to be in the a/c-phase, with regions where the *c* axis points out-of-plane (*c*-domains) as well as regions where it points in-plane (*a*-domains), giving rise to a ferroelastic a/c-domain configuration with 90° domain walls, as predicted in Ref. 3 and demonstrated experimentally (see, for example, Refs. 21–23).

As the in-plane lattice parameters of $DyScO_3$ are different along $[100]_{pc}$ ($a_{pc} = 3.974$ Å) and $[010]_{pc}$ ($b_{pc} = 3.951$ Å), the resulting epitaxial strain along these two axes is different too. The larger b_{pc} lattice parameter favors the *a*-domains to point with their polarization axis along $[010]_{pc}$, so-called a_2-domains, compared to a_1-domains with their polarization axis pointing along $[100]_{pc}$. This results in a domain configuration composed of a_1, a_2, and *c*-domains with different domain population ratios depending on the epitaxial strain and film thickness; for example, Damodaran *et al.*[24] showed that the domain configuration can be modified by the epitaxial strain, going from predominantly *c*-domains for $PbTiO_3$ grown on $SrTiO_3$ to a/c-domain structures on $DyScO_3$ to a more complex hierarchical domain architecture consisting of a mixture of a/c and a_1/a_2 domain structures when grown on $GdScO_3$. Langenberg *et al.*[25] observed, in $PbTiO_3$ grown by molecular beam epitaxy (MBE) onto different $(110)_o$ oriented rare-earth scandates, that the domain configuration can be effectively tuned by altering the strain and film thickness. For $PbTiO_3$ grown on $DyScO_3$, they observed the presence of a_2 and *c* domains for the thinner films, with a_1 domains appearing only for larger thicknesses. The formation of domain walls itself also costs energy. The domain wall nucleation was demonstrated to be very sensitive to the growth mode by Nesterov *et al.*:[22] in $PbTiO_3$ films grown on $DyScO_3$ by pulsed laser deposition (PLD), the presence or absence of a_1 domains can be controlled by the growth rate, with a_1, a_2, and *c* domains obtained for slow-grown films, while a_1 domains were absent for fast-grown films.

Additionally to these ferroelastic domains, the electrostatic boundary conditions also play a role. The polarization charges at the surface of the $PbTiO_3$ layers are partially screened[26–30] by charges in the $SrRuO_3$ layers. Bulk $SrRuO_3$ is a metallic transition-metal oxide and is often used as an electrode in the ferroelectric oxides community.[31] It is orthorhombic with room temperature *Pbnm* space group lattice parameters $a_o = 5.57$ Å, $b_o = 5.53$ Å, and $c_o = 7.85$ Å,[32] corresponding to the pseudocubic unit cell parameters $a_{pc} = c_{pc} = 3.924$ Å, $b_{pc} = 3.925$ Å, $\alpha_{pc} = \gamma_{pc} = 90°$, and $\beta_{pc} = 90.413°$. The depolarization field arising from the incomplete screening of the surface charges can lead the *c*-domains to split in alternating "up" (c^+) and "down" (c^-) domains with 180° domain walls and plays a role in the domain configuration for the thinner films. The combination of mechanical and electrostatic constraints can then result in flux-closure structures, as observed in tensile-strained $PbTiO_3$ thin films.[29,33,34]

We address the question of domain configuration and evolution as a function of the $PbTiO_3$ film thickness by using a combination of atomic force microscopy, laboratory and synchrotron x-ray diffraction, and high resolution scanning transmission electron microscopy. We observe the pattern visible at the surface of the $SrRuO_3/PbTiO_3/SrRuO_3$ heterostructures by atomic force microscopy (Sec. II A), while x-ray diffraction measurements are used to extract the domain periodicity (Sec. II B). We find that the anisotropic strain imposed by the orthorhombic $(110)_o$-oriented $DyScO_3$ substrate creates a large asymmetry in the domain configuration, with domain walls macroscopically aligned along one of the two in-plane directions. These measurements not only demonstrate that the evolution of the domain period with film thickness deviates from the Kittel law but also reveal an additional larger period appearing for the thicker films. The origin of this larger period is then investigated using scanning x-ray nanodiffraction microscopy with high spatial resolution, highlighting the arrangement of a/c domains into superdomains (Sec. II C). The evolution of the domain configuration with increasing film thickness from flux-closure-like to a/c domains is also demonstrated by direct imaging using transmission electron microscopy, where the arrangement of the a/c domains into superdomains is further confirmed (Sec. II D). Finally, we show that above a certain critical thickness, the large structural distortions associated with the ferroelastic domains propagate through the top $SrRuO_3$ layer, creating a modulated structure that extends beyond the ferroelectric layer thickness. The varying length scales of these periodic phenomena reveal the hierarchy of the different energy costs at play within the $PbTiO_3$ layers.

II. RESULTS

A. Periodic pattern at the surface of the heterostructures observed by atomic force microscopy

Atomic force microscopy (AFM) topography images obtained on the different samples reveal that as the $PbTiO_3$ layer thickness increases, trenches develop at the surface of the $SrRuO_3$ top

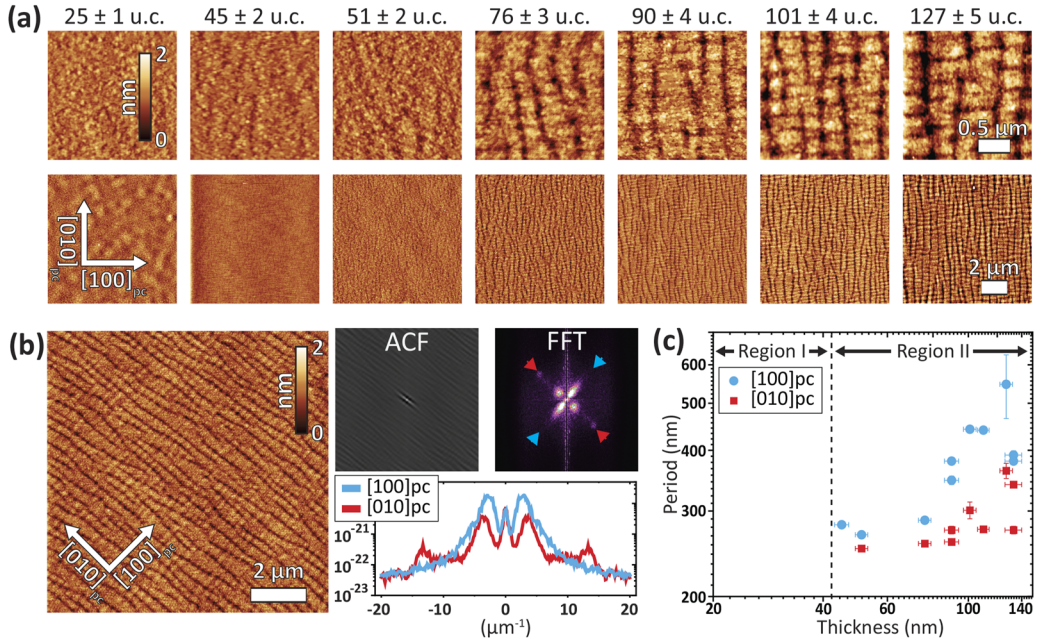

FIG. 1. (a) AFM topography images obtained on the different samples. The top rows are 2 × 2 μm^2 scans, and the bottom rows are 10 × 10 μm^2 scans, shown in the same 0–2 nm height scale. The orientation of each sample was fixed with respect to the substrate pseudo-cubic axes $[100]_{pc}$ and $[010]_{pc}$. From these images, it is clear that as the $PbTiO_3$ layer thickness increases, trenches develop on the surface of the $SrRuO_3$ top layer, with a pattern that gets more pronounced and anisotropic with thickness, with long and deep trenches parallel to the $[010]_{pc}$ axis, and smaller trenches parallel to the $[100]_{pc}$ axis. (b) Extracting the period for the 90 ± 4 u.c. thick $PbTiO_3$ layer using the Gwyddion software.[52] From the topography measurement, the autocorrelation function (ACF) is taken. A fast Fourier transform (FFT) is then applied, displaying periodic peaks along $[100]_{pc}$ and $[010]_{pc}$, clearly visible in the cuts, allowing us to determine the periodicity. (c) Evolution of the periodicity of the surface tilt pattern along the two crystallographic axis.

layer in an organized pattern (Fig. 1). For samples of 45 u.c. and below, this pattern is hardly visible, and the top $SrRuO_3$ is atomically flat. The pattern gets more pronounced and anisotropic with increasing $PbTiO_3$ layer thickness, with long and deep trenches parallel to the $[010]_{pc}$ axis, and smaller trenches parallel to the $[100]_{pc}$ axis, while the surface roughness stays reasonably low, with root mean square (rms) roughness values ranging from 157 to 393 pm over surfaces of 10 × 10 μm^2. The pattern that we observe at the surface of the $SrRuO_3$ top layer is comparable to what has been observed at the surface of $PbTiO_3$ layers grown on $DyScO_3$ substrates in Ref. 22 as a result of periodic ferroelastic a/c domains.

To extract the period of the distortions visible on the surface of the samples, we calculate the autocorrelation function (ACF) of the topography image and, subsequently, the fast Fourier transform (FFT) of the autocorrelation image, as shown in Fig. 1(b) for the sample with the 90 u.c. thick $PbTiO_3$ layer. As elaborated in Ref. 22, this method is more sensitive to the periodic distortions of the surface of the sample than a direct FFT of the topography image. The results for the different samples are shown in Fig. 1(c) and also reported in the concluding Fig. 5. Once visible, the periods along both directions ($[100]_{pc}$ and $[010]_{pc}$) increase as a function of the $PbTiO_3$ layer thickness, with the period along $[100]_{pc}$ being always larger than the period along $[010]_{pc}$.

B. Periodic patterns in the $PbTiO_3$ layers observed by x-ray diffraction

To relate this pattern observed at the surface of the $SrRuO_3$ layer to the domain pattern in the $PbTiO_3$ layers below, we used in-house x-ray diffraction to measure the reciprocal space maps (RSM) of our different samples (Fig. 2). For the thicker films, the butterfly shape—a signature of the a/c-phase—can be recognized, with the high intensity peak of the substrate overlapping with the peak of the a-domains and the peak of $SrRuO_3$. The peak of the c domains appears at a lower $Q_{[001]_{pc}}$ value. The butterfly wings arise from the tilts in the a- and c-domains.[35]

Comparing, in Fig. 2, the RSM obtained in the $Q_{[100]_{pc}}$–$Q_{[001]_{pc}}$ plane (top row) and in the $Q_{[010]_{pc}}$–$Q_{[001]_{pc}}$ plane (bottom row), we observe again an anisotropy between the two in-plane crystallographic axes $[100]_{pc}$ and $[010]_{pc}$: periodic peaks are clearly visible along $[010]_{pc}$, whereas the peaks along $[100]_{pc}$ are less well-defined and exhibit lower intensity. The position of these peaks was determined from intensity cuts at $Q_{[001]_{pc}}$ = 1.55 $Å^{-1}$, corresponding to the region of the c-domains, reported in Fig. 2(b) (see blue arrows). From the position of these peaks, we extracted the periodicity—plotted in blue in Fig. 2(c) as a function of the $PbTiO_3$ film thickness. The blue line serves as a guide to the eye and is obtained by fitting the evolution of the period p with film thickness

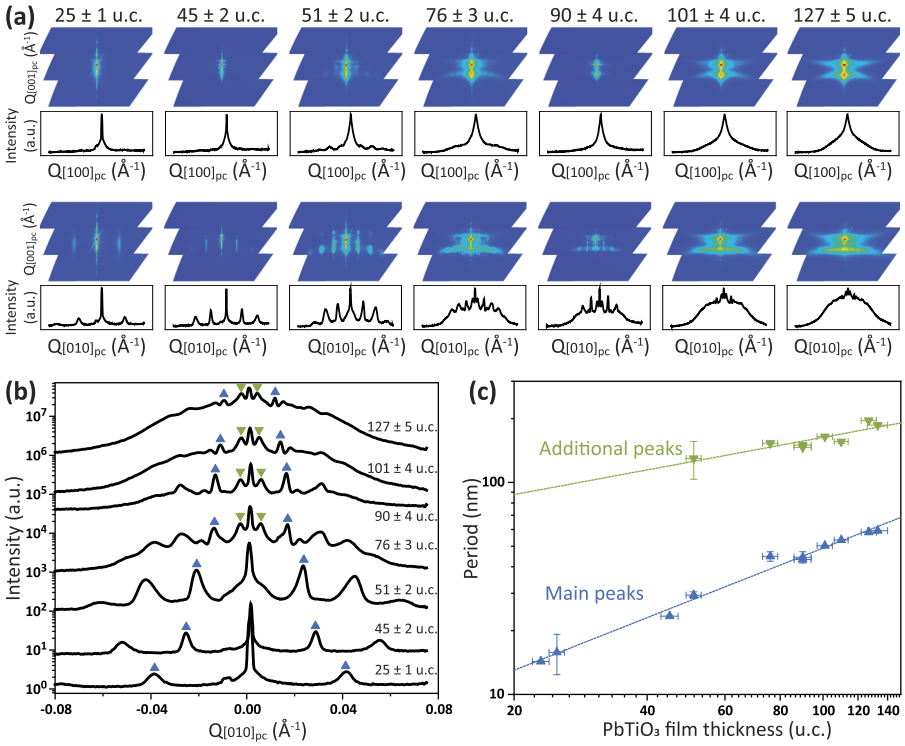

FIG. 2. (a) Reciprocal space maps (RSM) around the $(001)_{pc}$ peak of the substrate in the $Q_{[001]_{pc}} - Q_{[100]_{pc}}$ plane (top row) and in the $Q_{[001]_{pc}} - Q_{[010]_{pc}}$ plane (bottom row), for samples with different $PbTiO_3$ thicknesses. $Q_{[100]_{pc}}$ and $Q_{[010]_{pc}}$ vary from −0.1 to 0.1 Å^{-1}, while $Q_{[001]_{pc}}$ varies between 1.4 and 1.8 Å^{-1}. Below each map is the corresponding intensity obtained from a cut at $Q_{[001]_{pc}} = 1.55$ Å^{-1} (*c*-domains), displaying the periodic peaks originating from the domain pattern. These intensity cuts are reported in (b) for comparison, and the periods are plotted in (c)—see discussion in the text.

t using an exponential expression, $p = a \cdot t^n$. The best fit was obtained with $n = 0.8 \pm 0.1$, deviating from the Kittel law[36–41] where n should be equal to 1/2 (see Sec. III for a discussion regarding this deviation from the Kittel law).

Upon further analysis of the periodic peaks appearing in the RSM, we note, in Fig. 2(b), that additional peaks appear for the thicker films (see down-facing green triangles). These additional peaks correspond to larger periods, as reported in Fig. 2(c) in green. This time, the fit gives $n = 0.4 \pm 0.2$, much closer to what one would expect from the Kittel law. For comparison, we analyzed a 90 u.c. $PbTiO_3$ sample without the top $SrRuO_3$ electrode using piezoresponse force microscopy (PFM) measurements. We observed that in addition to the a/c domains, the out-of-plane polarization arranges into larger regions alternating between up and down polarization, forming c^+/c^- superdomains (see discussion in supplementary material Sec. S1 and in Ref. 42). The period of these superdomains matches with the value obtained from the additional peak in the RSM, confirming that the additional peaks come from the arrangement of the out-of-plane polarization in c^+/c^- superdomains. These additional peaks appear only for samples with a $PbTiO_3$ layer thicker than ~45 u.c., which is also the thickness above which the pattern starts to appear in the topography of the surface layer, as observed by AFM.

C. Tilts in *a*- and *c*-domains observed by synchrotron x-ray nanodiffraction

The 90 u.c. thick $PbTiO_3$ layer sample was also analyzed using scanning x-ray nanodiffraction microscopy (SXDM). This technique allows us to measure raster scans of local 3D-RSMs, with a spatial resolution determined by the focused x-ray beam size,[42] here ~30 × 30 nm^2 full width at half maximum (FWHM). The output of an SXDM map is thus the diffracted intensity I as a function of three reciprocal space coordinates ($Q_{[100]_{pc}}$, $Q_{[010]_{pc}}$, and $Q_{[001]_{pc}}$), and two direct space coordinates ($R_{[100]_{pc}}$ and $R_{[010]_{pc}}$) (Fig. 3).

The average 002 3D-RSM obtained by summing I over all sample positions ($R_{[100]_{pc}}$, $R_{[010]_{pc}}$) is shown in Fig. 3(a). The projections along $Q_{[010]_{pc}}$ and $Q_{[101]_{pc}}$ are shown in Figs. 3(b) and 3(c). This RSM displays the "butterfly" shape characteristic of the a/c phase already evident in Fig. 2. Compared to Fig. 2, however, in Figs. 3(a)–3(c), no satellites are present: because the domain period is comparable to the nanofocused beam size in a local 3D-RSM, the number of coherently illuminated periods is insufficient to give rise to the constructive interference that generates the satellites. The colored boxes in Figs. 3(b) and 3(c) define a region of interest (ROI), corresponding to an *a* or *c* domain tilted in one of the four $\langle 100 \rangle_{pc}$ directions. Along $Q_{[010]_{pc}}$ [Fig. 3(b)], we can identify the peaks of the a_2-domains with different tilts: a_I and a_{II}, and the correspondingly tilted *c*-domains

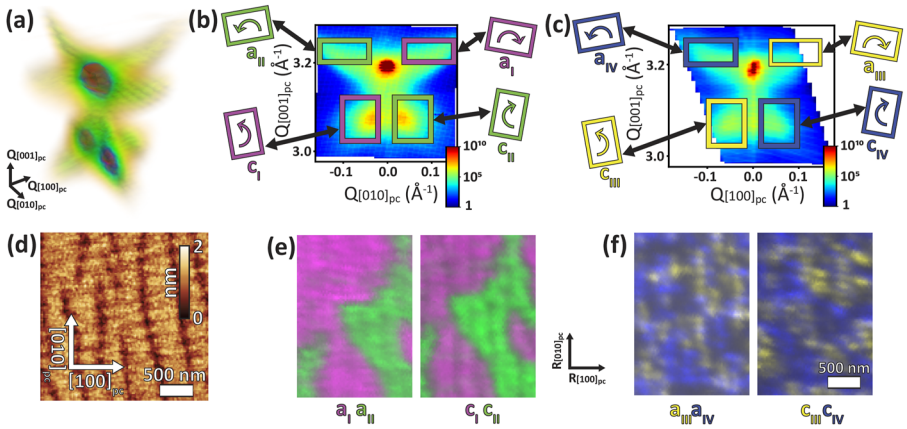

FIG. 3. Scanning x-ray diffraction microscopy of the 002 peak of a 90 ± 4 u.c. thick $PbTiO_3$ between the top and bottom $SrRuO_3$ electrodes (53 ± 2 u.c. thick) on a $DyScO_3$ substrate. (a) Average 002 3D-RSM calculated by summing all local 3D-RSMs collected at different sample positions within the SXDM raster scan. (b) and (c) Projection along $Q_{[100]_{pc}}$ (b) and $Q_{[010]_{pc}}$ (c) of the average 002 3D-RSM. Colored boxes define ROIs corresponding to *a* and *c* domains tilted in the four symmetrically equivalent $\langle 100 \rangle_{pc}$ directions. (d) Topography of this sample displayed in the same scale used in the spatial intensity maps for comparison. (e) and (f) Spatial maps of the sum of the intensity scattered within the ROIs defined in (b) and (c) using the corresponding color scale: in (e), the intensities corresponding to a_I (pink) and a_{II} (green) are overlaid using complementary colors; the same is done for c_I (pink) and c_{II} (green); in (f), a_{III} (yellow) and a_{IV} (blue) are overlaid; as for c_{III} (yellow) and c_{IV} (blue). Note that complementary colors are used, so that white (respectively black) corresponds to the superposition (respectively absence) of the two domains.

c_I and c_{II}. Similarly, along $Q_{[100]_{pc}}$ [Fig. 3(c)], we can identify the peaks of the a_1-domains with different tilts: a_{III} and a_{IV}, and the correspondingly tilted *c*-domains c_{III} and c_{IV}.

The sum of the intensity scattered within each ROI is computed for each local RSM and plotted as a function of $(R_{[100]_{pc}}, R_{[010]_{pc}})$ in Figs. 3(e) and 3(f). Here, each plot is labeled with the domain type and color of the respective ROI, allowing us to map the presence or absence of the different domains. Note that due to their small size, it is clusters, or "bundles" of domains rather than individual ones that are visible. By comparing the intensity maps to the topography of the sample displayed at the same scale in Fig. 3(d), one sees that the contrast is comparable, showing that the pattern observed in the topography of the $SrRuO_3$ top layer is related to the arrangement of the *a*/*c* domains in the $PbTiO_3$ layer below.

Comparing the *a* and *c* domain maps in Figs. 3(e) and 3(f), we see a clear correlation between the spatial distribution of different tilts: the spatial distribution of a_I domains matches that of the c_I domains (pink), the a_{II} of the c_{II} (green), the a_{III} of the c_{III} (yellow), and the a_{IV} of the c_{IV} (blue). Such pairing is to be expected given the crystallography of *a*/*c* twins.[44] More interestingly, a_I/c_I and a_{II}/c_{II} pairs appear to further aggregate at a larger scale into homogeneous areas, forming superdomains compatible with the observations in Figs. 2 and S1 (supplementary material).

D. Domain patterns in $PbTiO_3$ layers observed by transmission electron microscopy

A more direct way to image the domain structure is the use of cross-sectional scanning electron microscopy (STEM) (Fig. 4). Atomically resolved high angle annular dark field (HAADF)-STEM imaging allows us to observe the lattice and atomic displacements at the atomic level. The samples were cut and prepared for the STEM measurement so as to obtain slices in the plane defined by the $[010]_{pc}$ (horizontal direction) and $[001]_{pc}$ (vertical direction) axes of $DyScO_3$, imaging along the $[100]_{pc}$ zone-axis. In the 90 u.c. thick $PbTiO_3$ in Fig. 4, the *a*-domains are clearly visible as very narrow domains separated from the larger *c*-domains by domain walls in the $(011)_{pc}$ and $(0\bar{1}1)_{pc}$ planes.

Focusing on a region with the domain walls in the $(011)_{pc}$ planes [Fig. 4(c)], we observe the tilted *a* and *c*-domains, corresponding to an a_I-domain surrounded by c_I-domains. In the case of domain walls in the $(0\bar{1}1)_{pc}$ planes [Fig. 4(d)], we observe an a_{II}-domain surrounded by c_{II}-domains. These correspond to the a_I/c_I and a_{II}/c_{II} pairing observed in the nanodiffraction data (Fig. 3).

Interestingly, in these two different regions, the polarization in the *c*-domains is always oriented down (in the $[001]_{pc}$ direction), while the polarization in the *a*-domains is always oriented to the right (in the $[010]_{pc}$ direction).

At a larger scale, the periodic pattern is directly visible in real space, and the period can be estimated by taking the FFT of the image, as shown in Fig. 4(f). Looking at the $(001)_{pc}$ Bragg spot in the obtained reciprocal space map [Fig. 4(g)], one can see the superstructure with a periodicity corresponding to 40–45 nm, in perfect agreement with the values obtained from the RSM (see Fig. 5 for the comparison between values obtained by the different techniques).

In Fig. 4(g), one also recognizes the butterfly shape as observed by XRD and nanodiffraction. By selecting different regions of interest, it is then possible to reconstruct the direct space images in Figs. 4(h) and 4(i), revealing the mapping of the *a* and *c*-domains (a_I and c_I in pink, a_{II} and c_{II} in green). Although the reconstructed image is sharper for the *a*-domains [Fig. 4(h)] than for the *c*-domains [Fig. 4(i)], it allows us to confirm at a local scale and with direct imaging the result obtained by nanodiffraction: the *a* and *c*-domains organize themselves, not only in pairs but also in larger regions composed of several a_I/c_I pairs alternating with larger regions composed of several a_{II}/c_{II} pairs, forming superdomain structures.

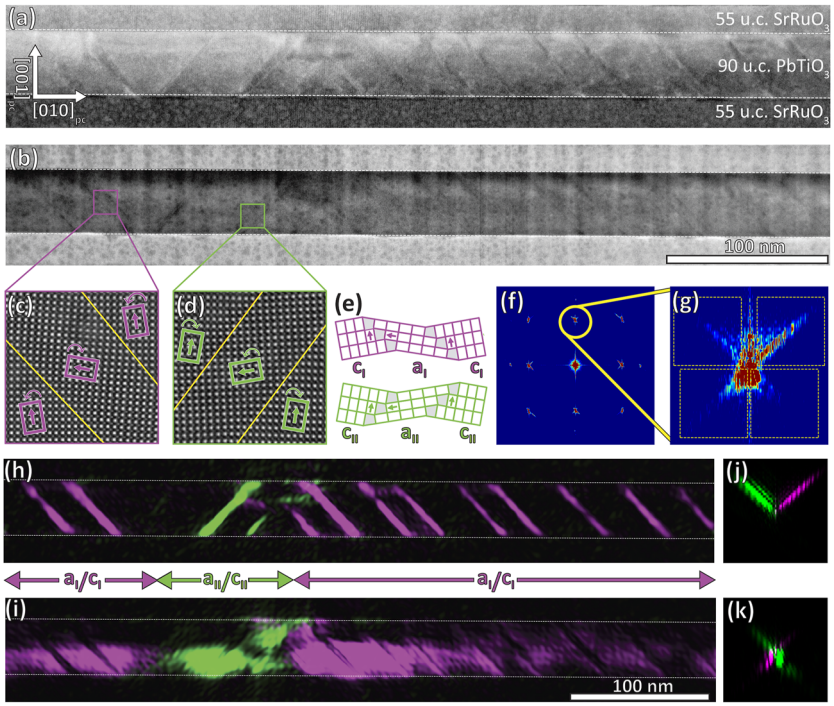

FIG. 4. STEM image of a 90 ± 4 u.c. thick $PbTiO_3$ between the top and bottom $SrRuO_3$ electrodes (53 ± 2 u.c. thick) on $DyScO_3$ substrate. (a-b) Low magnification bright field (BF) (a) and medium angle annular dark field (MAADF) (b) images revealing the a/c phase of the $PbTiO_3$ layer, with the a/c domain walls inclined in the $(011)_{pc}$ or $(0\bar{1}1)_{pc}$ planes. (c) and (d) High resolution images around two *a*-domains with different domain wall orientations, showing a_I and c_I domains separated by domain walls in the $(011)_{pc}$ planes (c), and a_{II} and c_{II} domains separated by domain walls in the $(0\bar{1}1)_{pc}$ planes (d). The arrows indicate the Ti displacements. (e) Schematic representation of the domain pairs. (f) FFT pattern of the $PbTiO_3$ layer where the butterfly shape of the $(001)_{pc}$ is highlighted in (g). Squares in (g) represent the regions of interest used for the image reconstruction, the top squares corresponding to signal from *a*-domains, and the bottom ones from the *c*-domains. (h-i) Images reconstructed from the intensity of the FFT filtered pattern for the *a*-domains (h) and *c*-domains (i). (j-k) FFTs for areas corresponding to a_I and a_{II} domains are overlapped in (j), and c_I and c_{II} in (k).

III. DISCUSSION

The different periods observed in this work along $[010]_{pc}$ from the AFM topography, the RSM, and the STEM images are summarized in Fig. 5(d). From this Figure, we see that two different regions can be defined: region I where no pattern is visible in the topography for the thinner $PbTiO_3$ films (45 u.c. and lower), and region II where the topography displays tilts and trenches, and where additional peaks appear in the RSM for the thicker $PbTiO_3$ films (50 u.c. and higher).

In the STEM images [Figs. 5(a)–5(c)], the domain walls are visible in the $PbTiO_3$ layers. The sample in region II has a clear a/c-phase domain structure [Fig. 5(a)], while the two samples measured in region I show a more complex domain pattern [Figs. 5(b) and 5(c)], sharing similarities with the flux-closure like pattern observed in $PbTiO_3/SrTiO_3$ heterostructures on $GdScO_3$.[33] We extracted the periodicity of these different domain configurations by performing FFT filtering and found 40–45 nm for the 90 u.c. thick $PbTiO_3$, 25–30 nm for the 45 u.c. thick $PbTiO_3$, and 16 nm for the 23 u.c. thick $PbTiO_3$, in perfect agreement with the values obtained from the RSM [see Fig. 5(d) - black dots].

Looking at the evolution of the periods as a function of film thickness, we observe that the period of the ferroelastic domain structure in the $PbTiO_3$ layers (blue triangles and black dots) decreases with decreasing film thickness. When considering the energetics at play in ferroelastic domains in epitaxial ferroelectric and ferroelastic films, Pertsev and Zembilgotov[41] showed that the dependence of the equilibrium domain period on film thickness varies from linear to the usual square root law at very large film thickness, as the domain wall energy density varies with film thickness. At very low thicknesses, the domain size can even increase as the film thickness is reduced.[41,45,46] In our work, we did not observe such a turnover of domain size for our samples within the studied thickness range, but rather a continuous decrease of periodicity p with decreasing film thickness t through both regions as $p \sim t^n$ with $n = 0.8 \pm 0.1$, following an intermediate behavior between Kittel's square-root law[36–41] and Pertsev's linear law.[41] This is very close to the value obtained by Nesterov *et al.*[22] ($n = 0.68 \pm 0.3$). It also compares well with the results obtained in different works on $PbTiO_3$ epitaxially strained to $DyScO_3$,[8,9,12,13,18] as reported in the supplementary material (Sec. S2). Interestingly, this scaling is also observed in other materials: in $K_{0.9}Na_{0.1}NbO_3$ thin films epitaxially strained to (110)-$NdScO_3$, the domain period scales with an exponent $n = 0.8 \pm 0.1$ across a range of film thicknesses and domain structures, from in-plane a_1/a_2 domains for very thin films, to the onset of a ferroelectric monoclinic M_C phase at larger

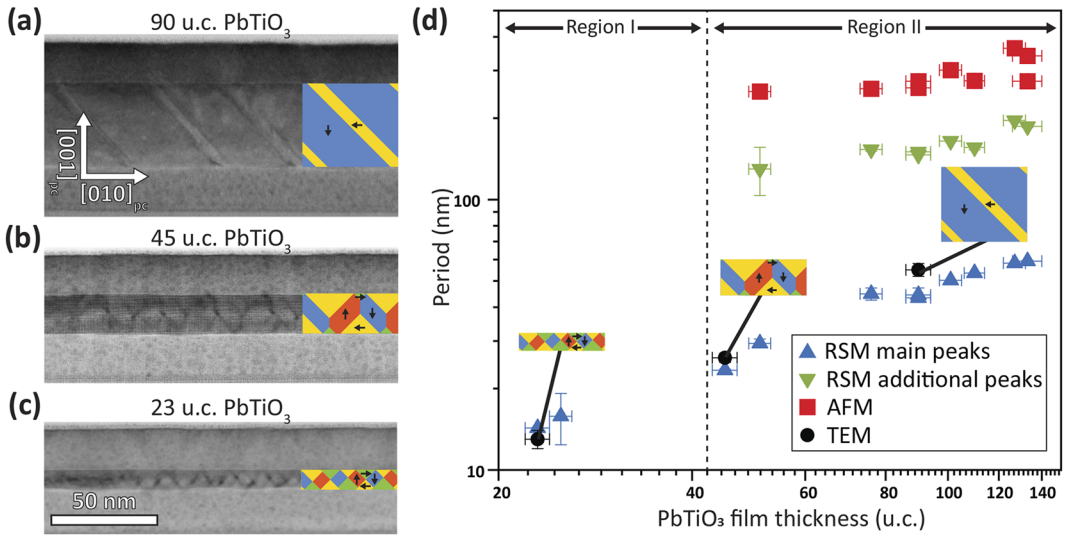

FIG. 5. Summary of the domain evolution along $[010]_{pc}$ as a function of $PbTiO_3$ thickness. (a)–(c) STEM-BF images revealing the domain walls and domain pattern evolution from flux-closure like to a/c as the $PbTiO_3$ film thickness increases. (d) Evolution of the periods obtained from the AFM topography images (red dots), via RSM (blue and green triangles for the main period and additional period respectively), and from STEM images (purple diamonds). From this Figure, we see a good match between the values obtained by STEM and RSM. We also see that two different regions can be defined: one region where no pattern is visible in the topography and no additional peaks appear in the RSM for the thinner $PbTiO_3$ films (45 u.c. and lower), and one region where the topography displays tilts and trenches, and where additional peaks appear in the RSM for the thicker $PbTiO_3$ films (50 u.c. and higher).

film thickness, accompanied by a transformation of the domain configuration from stripe domains to a herringbone pattern and then eventually to a checkerboard pattern as the film thickness increases from 10 to 60 nm.[47]

In region II, where the samples are in the a/c-phase, an additional periodicity appears, which is observed in XRD as additional periodic peaks. The evolution of this superdomain period is closer to the Kittel square-root law [Fig. 5(d)]. Nanodiffraction measurements and STEM allowed us to spatially resolve the a/c pattern in the sample with 90 u.c. thick $PbTiO_3$ and to demonstrate the coupling of the tilts of the a- and c-domains, revealing the organization of these domains at a larger scale: the a/c-domains organize in "superdomains," i.e., regions composed of either a_I/c_I, a_{II}/c_{II}, a_{III}/c_{III}, or a_{IV}/c_{IV} domains. This gives rise to an additional periodicity that can be detected as additional peaks in the RSM. From the PFM measurements on a sample without the top $SrRuO_3$ electrode, we relate these additional periodic peaks to the 180° ferroelectric domains (c^+/c^-), where the out-of-plane polarization alternates between up and down, in a configuration determined by the screening of the depolarization field and electrostatic boundary conditions. Although we could not confirm it directly, one possibility is that these c^+/c^- domains correspond to the superdomains observed with different a/c tilts.

In region I, the domains form a complex polarization texture, similar to the flux-closure pattern, with a period following the behavior of the a/c-domain pattern at a larger thickness and without any additional peaks or superdomain structure. The different polarization patterns appearing at the different thicknesses are the result of the best compromise to accommodate the cost of strain and depolarization field at the same time. This explains why, in this regime, it is possible to observe very complex patterns, such as flux-closure,[12,33] vortices,[8,9,18] supercrystals,[12] and incommensurate spin (polarization) structures,[13] all with the period determined by the strain from the substrate and the layer thickness.

IV. CONCLUSION

Our work demonstrates the presence of two regimes with different ferroelectric/ferroelastic domain configurations. For the smaller $PbTiO_3$ thicknesses, the combination of the effect of strain and electrostatic boundary conditions gives rise to a complex domain configuration where flux-closure, vortices, or supercrystal configurations can develop. For larger $PbTiO_3$ thicknesses, the a/c-phase induced by epitaxial strain is recovered, with large superdomains appearing to screen the depolarization field. The large structural distortions associated with the ferroelastic domains propagate through the top $SrRuO_3$ layer, creating a modulated structure that extends beyond the ferroelectric layer thickness and allowing for domain engineering in the top $SrRuO_3$ electrode.[48] These domain structures not only change the properties of the ferroelectric itself but can also be used to change the properties of other materials through electrostatic and structural coupling.

V. EXPERIMENTAL TECHNIQUES

A. Sample growth

All the samples were deposited using our in-house constructed off-axis radio-frequency magnetron sputtering system, which was

equipped with three different guns allowing the deposition of heterostructures and solid-solutions of high crystalline quality composed of up to three different materials: $PbTiO_3$, $SrTiO_3$, and $SrRuO_3$. $PbTiO_3$ thin films are typically deposited around 560 and 580 °C, in 180 mTorr of a 20:29 O_2/Ar mixture, at a power of 60 W, and using a $Pb_{1.1}TiO_3$ target with 10% excess of Pb to compensate for its volatility. $SrRuO_3$ electrodes were deposited *in situ* from a stoichiometric target at 640 °C in 100 mTorr of O_2/Ar mixture of ratio 3:60 at a power of 80 W. Huettinger PFG 300 RF power supplies are used in power control mode. The sample holder is grounded during deposition, but the sample surface is left floating.

B. Atomic force microscopy

Topography measurements were performed using a *Digital Instrument* Nanoscope Multimode DI4 with a *Nanonis* controller. Piezoresponse force microscopy measurements under ambient conditions to image the intrinsic domain patterns were performed on an *Asylum Research Cypher* or *MFP-3D* atomic force microscopes.

C. X-ray diffraction

In-house XRD measurements were performed using a *Panalytical X'Pert* diffractometer with Cu Kα_1 radiation (1.540 598 0 Å) equipped with a 2-bounce Ge(220) monochromator and a triple axis detector in our laboratory in Geneva. The θ–2θ scans were analyzed using the *InteractiveXRDFit* software.[48] This XRD system is also equipped with a PIXcel1D detector, which is used for faster acquisition of the reciprocal space maps.

The 90 u.c. thick $PbTiO_3$ layer sample was further analyzed using scanning x-ray diffraction microscopy (SXDM)[42] on the ID01 beamline at the European Synchrotron Radiation Facility (ESRF).[50] An incident x-ray energy of 9.5 keV was selected using a Si(111) double crystal monochromator with resolution $\Delta\lambda/\lambda = 10^{-4}$. A 0.7 μm-thick tungsten Fresnel zone plate with a 300 μm diameter and a 20 nm outer zone width was used to focus the x-ray beam down to a spot size of $\sim 30 \times 30$ nm^2 FWHM, as measured via a ptychography scan of a known reference object.[50] The sample was placed at the 002 diffraction condition and raster scanned relative to the focused beam in 25 nm steps over a 4×4 μm^2 area using a commercial piezo scanner. A two-dimensional MAXIPIX detector positioned ~0.4 m downstream of the sample stage was exposed for 12 ms at each sample position. The procedure was repeated at different incidence angles about the 002 condition to obtain a 5-dimensional dataset describing the diffracted intensity as a function of three reciprocal and two direct space dimensions, i.e., $I(Q_{[100]_{pc}}, Q_{[010]_{pc}}, Q_{[001]_{pc}}, R_{[100]_{pc}}, R_{[010]_{pc}})$. We note that reaching the 002 diffraction condition entails forming a ~19° angle with the (00L) planes; since the measurements were performed with an x-ray beam parallel to $[100]_{pc}$, the direct space resolution is degraded along this direction, and features appear elongated parallel to it.

D. Scanning transmission electron microscopy

Cross-sectional lamella prepared by a focus ion beam allows the imaging of domain structures by scanning transmission electron microscopy (STEM). Experiments were acquired on Nion Cs-corrected UltraSTEM200 at 100 kV operating voltage. A convergence angle of 30 mrad was used to allow high-resolution atomic imaging with a typical spatial resolution of 1 Å. Three imaging detectors in the STEM are used to simultaneously obtain bright field (BF), annular bright field (ABF) or medium angle annular dark field (MAADF), and high angle annular dark field (HAADF) images.

For ABF-MAADF imaging, the inner-outer angles can be continuously adjusted between 10 and 20 to 60–120 mrad. Most ABF images were collected with 15–30 mrad and MAADF images with 40–80 mrad angular ranges.

We determine the periodicity of the superstructures in the $PbTiO_3$ layer by measuring the distances between the additional reciprocal space spots obtained after FFT. The accuracy of the measurement was estimated by considering the diffraction spot extension as the lower and upper limit for the superstructure length estimation.

SUPPLEMENTARY MATERIAL

The supplementary material includes a discussion about the observation of c^+/c^- superdomains in a sample without the top $SrRuO_3$ electrode (Sec. S1) and a discussion about deviation from Kittel law, with the comparison with ferroelastic and flux-closure domains in other $PbTiO_3$ thin films and superlattices on $DyScO_3$ (Sec. S2).

ACKNOWLEDGMENTS

The authors thank Kumara Cordero-Edwards and Christian Weymann for their support and discussions. This work was supported by the Division II of the Swiss National Science Foundation under Project No. 200021_200636. STEM experiments were supported by the EU Horizon research and innovation program under Grant Agreement ID 823717-ESTEEM3. M.H. acknowledges funding from the SNSF Scientific Exchanges Scheme (Grant No. IZSEZ0_212990).

AUTHOR DECLARATIONS

Conflict of Interest

The authors have no conflicts to disclose.

Author Contributions

C.L., M.H., P.P., A.G., and J.-M.T. designed the experiment. C.L., M.H., and L.T. grew the samples and conducted the AFM and XRD measurements and analysis. E.Z. conducted the synchrotron x-ray nanodiffraction measurements and analysis. C.-P.S. and A.G. conducted the STEM measurements and analysis. I.G. performed additional STEM analysis. C.L., M.H., I.G., and P.P. wrote the manuscript with contributions from all authors. All authors discussed the experimental results and models, commented on the manuscript, and agreed on its final version.

Céline Lichtensteiger: Conceptualization (equal); Data curation (equal); Formal analysis (equal); Funding acquisition (equal); Investigation (equal); Methodology (equal); Project administration

(equal); Resources (equal); Software (equal); Supervision (equal); Validation (equal); Visualization (equal); Writing – original draft (equal); Writing – review & editing (equal). **Marios Hadjimichael**: Conceptualization (equal); Data curation (equal); Formal analysis (equal); Investigation (equal); Methodology (equal); Validation (equal); Visualization (equal); Writing – original draft (equal); Writing – review & editing (equal). **Edoardo Zatterin**: Data curation (equal); Formal analysis (equal); Investigation (equal); Resources (equal); Software (equal); Writing – original draft (equal); Writing – review & editing (equal). **Chia-Ping Su**: Investigation (equal); Methodology (equal); Resources (equal); Software (equal); Writing – original draft (equal); Writing – review & editing (equal). **Iaroslav Gaponenko**: Data curation (equal); Formal analysis (equal); Investigation (equal); Software (equal); Validation (equal); Visualization (equal); Writing – original draft (equal); Writing – review & editing (equal). **Ludovica Tovaglieri**: Data curation (equal); Formal analysis (equal); Investigation (equal); Writing – original draft (equal); Writing – review & editing (equal). **Patrycja Paruch**: Conceptualization (equal); Funding acquisition (equal); Writing – original draft (equal); Writing – review & editing (equal). **Alexandre Gloter**: Conceptualization (equal); Funding acquisition (equal); Supervision (equal); Writing – original draft (equal); Writing – review & editing (equal). **Jean-Marc Triscone**: Conceptualization (equal); Funding acquisition (equal); Supervision (equal); Writing – review & editing (equal).

DATA AVAILABILITY

The data that support the findings of this study are openly available in Yareta at https://doi.org/10.26037/yareta:7eof5tfyjrdpblws5vsqrvf3ny.

REFERENCES

[1] N. A. Pertsev, A. G. Zembilgotov, and A. K. Tagantsev, "Effect of mechanical boundary conditions on phase diagrams of epitaxial ferroelectric thin films," Phys. Rev. Lett. **80**, 1988–1991 (1998).

[2] N. A. Pertsev and V. G. Koukhar, "Polarization instability in polydomain ferroelectric epitaxial thin films and the formation of heterophase structures," Phys. Rev. Lett. **84**, 3722 (2000).

[3] V. G. Koukhar, N. A. Pertsev, and R. Waser, "Thermodynamic theory of epitaxial ferroelectric thin films with dense domain structures," Phys. Rev. B **64**, 214103 (2001).

[4] Y. L. Li, S. Y. Hu, Z. K. Liu, and L. Q. Chen, "Phase-field model of domain structures in ferroelectric thin films," Appl. Phys. Lett. **78**, 3878–3880 (2001).

[5] Z. Jiang *et al.*, "Strain-induced control of domain wall morphology in ultrathin $PbTiO_3$ films," Phys. Rev. B **89**, 214113 (2014).

[6] J. B. J. Chapman, A. V. Kimmel, and D. M. Duffy, "Novel high-temperature ferroelectric domain morphology in $PbTiO_3$ ultrathin films," Phys. Chem. Chem. Phys. **19**, 4243–4250 (2017).

[7] D. G. Schlom *et al.*, "Strain tuning of ferroelectric thin films," Annu. Rev. Mater. Res. **37**, 589–626 (2007).

[8] A. K. Yadav *et al.*, "Observation of polar vortices in oxide superlattices," Nature **530**, 198–201 (2016).

[9] P. Shafer *et al.*, "Emergent chirality in the electric polarization texture of titanate superlattices," Proc. Natl. Acad. Sci. U. S. A. **115**, 915–920 (2018).

[10] V. A. Stoica *et al.*, "Optical creation of a supercrystal with three-dimensional nanoscale periodicity," Nat. Mater. **18**, 377–383 (2019).

[11] M. Hadjimichael, "Ferroelectric domains in lead titanate heterostructures," Ph.D. thesis, University College London, 2019.

[12] M. Hadjimichael *et al.*, "Metal–ferroelectric supercrystals with periodically curved metallic layers," Nat. Mater. **20**, 495–502 (2021).

[13] D. Rusu *et al.*, "Ferroelectric incommensurate spin crystals," Nature **602**, 240–244 (2022).

[14] M. A. Pereira Gonçalves, C. Escorihuela-Sayalero, P. Garca-Fernández, J. Junquera, and J. Íñiguez, "Theoretical guidelines to create and tune electric skyrmion bubbles," Sci. Adv. **5**, eaau7023 (2019).

[15] S. Das *et al.*, "Observation of room-temperature polar skyrmions," Nature **568**, 368–372 (2019).

[16] Y. J. Wang *et al.*, "Polar meron lattice in strained oxide ferroelectrics," Nat. Mater. **19**, 881 (2020).

[17] J. Íñiguez, P. Zubko, I. Luk'yanchuk, and A. Cano, "Ferroelectric negative capacitance," Nat. Rev. Mater. **4**, 243 (2019).

[18] A. R. Damodaran *et al.*, "Phase coexistence and electric-field control of toroidal order in oxide superlattices," Nat. Mater. **16**, 1003–1009 (2017).

[19] G. Shirane, R. Pepinsky, and B. C. Frazer, "X-ray and neutron diffraction study of ferroelectric $PbTiO_3$," Acta Crystallogr. **9**, 131–140 (1956).

[20] B. Veličkov, V. Kahlenberg, R. Bertram, and M. Bernhagen, "Crystal chemistry of $GdScO_3$, $DyScO_3$, $SmScO_3$ and $NdScO_3$," Z. Kristallogr. **222**, 466–473 (2007).

[21] G. Catalan *et al.*, "Flexoelectric rotation of polarization in ferroelectric thin films," Nat. Mater. **10**, 963–967 (2011).

[22] O. Nesterov *et al.*, "Thickness scaling of ferroelastic domains in $PbTiO_3$ films on $DyScO_3$," Appl. Phys. Lett. **103**, 142901 (2013).

[23] M. J. Highland *et al.*, "Interfacial charge and strain effects on the ferroelectric behavior of epitaxial (001) $PbTiO_3$ films on (110) $DyScO_3$ substrates," Appl. Phys. Lett. **104**, 132901 (2014).

[24] A. R. Damodaran *et al.*, "Three-state ferroelastic switching and large electromechanical responses in $PbTiO_3$ thin films," Adv. Mater. **29**, 1702069 (2017).

[25] E. Langenberg *et al.*, "Strain-engineered ferroelastic structures in $PbTiO_3$ films and their control by electric fields," ACS Appl. Mater. Interfaces **12**, 20691–20703 (2020).

[26] J. Junquera and P. Ghosez, "Critical thickness for ferroelectricity in perovskite ultrathin films," Nature **422**, 506–509 (2003).

[27] P. Aguado-Puente and J. Junquera, "Ferromagneticlike closure domains in ferroelectric ultrathin films: First-principles simulations," Phys. Rev. Lett. **100**, 177601 (2008).

[28] M. Stengel, D. Vanderbilt, and N. A. Spaldin, "Enhancement of ferroelectricity at metal-oxide interfaces," Nat. Mater. **8**, 392–397 (2009).

[29] S. Li *et al.*, "Periodic arrays of flux-closure domains in ferroelectric thin films with oxide electrodes," Appl. Phys. Lett. **111**, 052901 (2017).

[30] M. Hadjimichael, Y. Li, L. Yedra, B. Dkhil, and P. Zubko, "Domain structure and dielectric properties of metal-ferroelectric superlattices with asymmetric interfaces," Phys. Rev. Mater. **4**, 094415 (2020).

[31] C. B. Eom *et al.*, "Single-crystal epitaxial thin films of the isotropic metallic oxides $Sr_{1-x}Ca_xRuO_3$ ($0 \le x \le 1$)," Science **258**, 1766–1769 (1992).

[32] J. J. Randall and R. Ward, "The preparation of some ternary oxides of the platinum metals," J. Am. Chem. Soc. **81**, 2629–2631 (1959).

[33] Y. L. Tang *et al.*, "Observation of a periodic array of flux-closure quadrants in strained ferroelectric $PbTiO_3$ films," Science **348**, 547–551 (2015).

[34] S. Li *et al.*, "Evolution of flux-closure domain arrays in oxide multilayers with misfit strain," Acta Mater. **171**, 176–183 (2019).

[35] K. Lee and S. Baik, "Ferroelastic domain structure and switching in epitaxial ferroelectric thin films," Annu. Rev. Mater. Res. **36**, 81–116 (2006).

[36] L. Landau, E. Lifshitz, and E. M. Lifšic, *On the Theory of the Dispersion of Magnetic Permeability in Ferromagnetic Bodies* (Pergamon Press, Oxford, 1992).

[37] C. Kittel, "Theory of the structure of ferromagnetic domains in films and small particles," Phys. Rev. **70**, 965–971 (1946).

[38] T. Mitsui and J. Furuichi, "Domain structure of Rochelle salt and KH_2PO_4," Phys. Rev. **90**, 193–202 (1953).

[39] A. L. Roitburd, "Equilibrium structure of epitaxial layers," Phys. Status Solidi A **37**, 329–339 (1976).

[40] W. Pompe, X. Gong, Z. Suo, and J. S. Speck, "Elastic energy release due to domain formation in the strained epitaxy of ferroelectric and ferroelastic films," J. Appl. Phys. **74**, 6012–6019 (1993).

[41] N. A. Pertsev and A. G. Zembilgotov, "Energetics and geometry of 90° domain structures in epitaxial ferroelectric and ferroelastic films," J. Appl. Phys. **78**, 6170–6180 (1995).
[42] L. Tovaglieri *et al.*, "Ferroelastic/ferroelectric superdomains pattern in epitaxially strained $PbTiO_3$ heterostructures observed by piezo-response force microscopy," (unpublished) (2023).
[43] M. Hadjimichael, E. Zatterin, S. Fernandez-Peña, S. J. Leake, and P. Zubko, "Domain wall orientations in ferroelectric superlattices probed with synchrotron X-ray diffraction," Phys. Rev. Lett. **120**, 037602 (2018).
[44] J. S. Speck, A. C. Daykin, A. Seifert, A. E. Romanov, and W. Pompe, "Domain configurations due to multiple misfit relaxation mechanisms in epitaxial ferroelectric thin films. III. Interfacial defects and domain misorientations," J. Appl. Phys. **78**, 1696–1706 (1995).
[45] A. Kopal, T. Bahnik, and J. Fousek, "Domain formation in thin ferroelectric films: The role of depolarization energy," Ferroelectrics **202**, 267–274 (1997).
[46] C. W. Huang, Z. H. Chen, and L. Chen, "Thickness-dependent evolutions of domain configuration and size in ferroelectric and ferroelectric-ferroelastic films," J. Appl. Phys. **113**, 094101 (2013).
[47] D. Braun, M. Schmidbauer, M. Hanke, and J. Schwarzkopf, "Hierarchy and scaling behavior of multi-rank domain patterns in ferroelectric $K_{0.9}Na_{0.1}NbO_3$ strained films," Nanotechnology **29**, 015701 (2018).
[48] C. Lichtensteiger *et al.*, "Nanoscale domain engineering in $SrRuO_3$ thin films," (unpublished) (2023).
[49] C. Lichtensteiger, "*InteractiveXRDFit*: A new tool to simulate and fit X-ray diffractograms of oxide thin films and heterostructures," J. Appl. Crystallogr. **51**, 1745–1751 (2018).
[50] S. J. Leake *et al.*, "The nanodiffraction beamline ID01/ESRF: A microscope for imaging strain and structure," J. Synchrotron Radiat. **26**, 571–584 (2019).
[51] D. Nečas and P. Klapetek, "Gwyddion: An open-source software for SPM data analysis," Cent. Eur. J. Phys. **10**, 181–188 (2012).